BioNanoSci.
DOI 10.1007/s12668-011-0003-8

Dynamic Failure of a Lamina Meshwork in Cell Nuclei under Extreme Mechanical Deformation

Zhao Qin · Markus J. Buehler

Abstract The nuclear lamina is a structural protein meshwork at the inner nuclear membrane. It confers mechanical strength to the cell's nucleus and also sustains the overall structural integrity of the cell. The rupture of nuclear lamina is involved in many physiologically extreme conditions, such as cell division, genetic disease, and injury. Yet, its rupture mechanisms and processes are largely unknown and failure models commonly used for engineering materials cannot be directly applied due to the complex hierarchical structure. Here, we use a multiscale modeling technique to investigate the dynamic failure of the nuclear lamina meshwork from the bottom up. We find that flaws or cracks in the nuclear lamina act as seeds for catastrophic failure that propagate rapidly upon very large deformation. Fracture occurs via crack propagation at intersonic speeds, and greater than the Rayleigh-wave speed predicted as a limit by classical fracture theory but smaller than the longitudinal wave speed. Our analysis shows that nanoscale secondary structural changes in protein filaments such as the alpha–beta transition and intermolecular sliding explain this macroscale phenomenon. Based on a simple model, we discover that the crack propagation speed is governed by the square root of the ratio of the tangent material moduli in (E_x) and perpendicular (E_y) to the crack propagation direction, $v \sim \sqrt{E_x/E_y}$ where the relative levels of applied strains in the x- and y-direction control the crack speed.

Z. Qin · M. J. Buehler (✉)
Laboratory for Atomistic and Molecular Mechanics,
Department of Civil and Environmental Engineering,
Massachusetts Institute of Technology,
77 Mass. Ave. Room 1-235A&B,
Cambridge, MA 02139, USA
e-mail: mbuehler@MIT.EDU

Published online: 30 April 2011

Keywords Nuclear lamina · Intermediate filament meshwork · Biological material · Multi-scale modeling · Failure · Materiomics

1 Introduction

The term intermediate filament refers to a heterogeneous family of cytoskeletal and nuclear skeletal proteins with the ability to self-assemble into ≈10-nm-wide filaments [1–4]. The name was coined back in 1968 because their diameters appeared to be intermediate in size between those of two other prominent cellular components, microtubules and microfilaments [3]. Intermediate filaments are fibrous proteins that are absent from both plants and fungi, but found widely in animals; and they are linked to several human diseases [5–8]. Lamin is a type of intermediate filament that is found in the nuclear lamina meshwork, which is a key building block that maintains the integrity of the cell's nuclear envelope [2]. The nuclear lamina features high strength and extensibility, enabling it to protect the genetic material inside the nucleus from damage. However, physiologically extreme conditions, including contraction of muscular cells, depolymerization during cell division, the exposition to ionizing radiation, and genetic mutations, can lead to flaws and defects within the meshwork structure. Accumulated flaws can result in the generation of crack-like defects as shown in earlier experimental work [9].

Much attention has been paid to the physiological characteristics of the nuclear lamina, and especially to the factors that affect the stability of the nuclear envelope. The nuclear lamina is found to be highly mutation sensitive, and a complex set of more than 13 different human diseases including Hutchinson–Gilford progeria syndrome (rapid-aging disease) [5, 6, 8] is found in humans. For example, the rapid-aging disease originates from a point mutation at the tail domain of the lamin

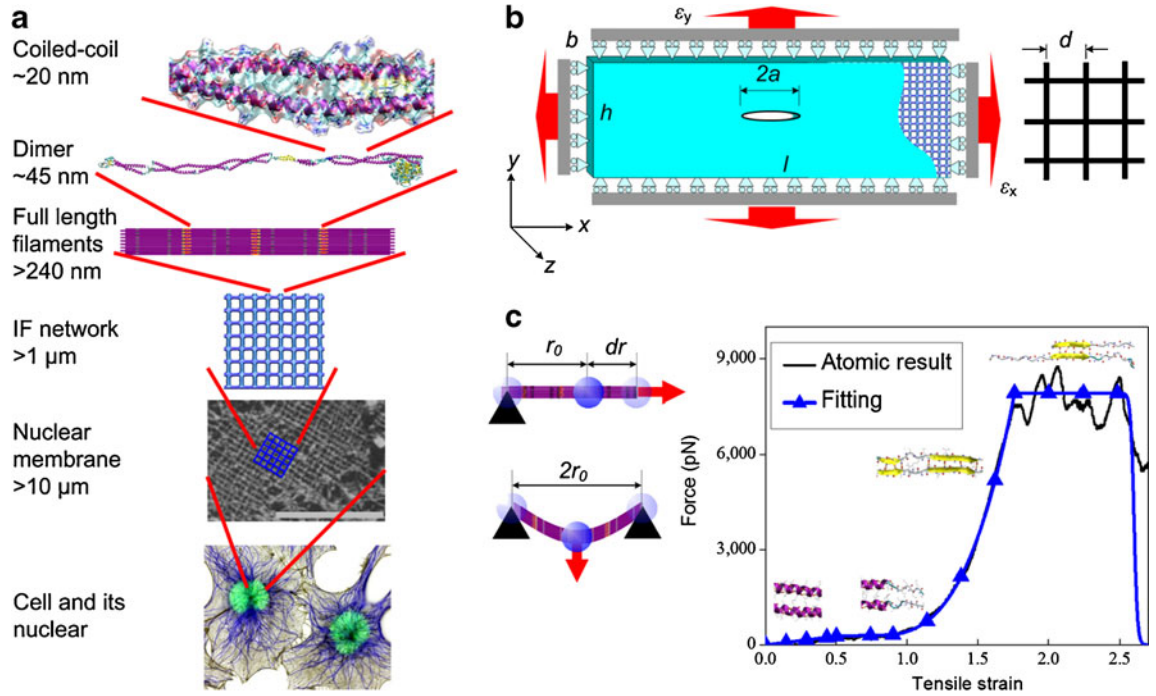

Fig. 1 Hierarchical structure of an intermediate filament meshwork as found in the inner layer of nuclear envelope of *Xenopus* oocytes, boundary conditions in simulations, geometry of the meshwork model and tensile properties of a single intermediate filament. **a** Schematic of the hierarchical intermediate filament structure that ranges from nano to macro. Panel **a** shows typical structural features of intermediate filament meshwork, including hydrogen bonds, coiled-coil composed of alpha-helix, a lamin A dimer composed of coiled-coil and linkers, bundles of dimers that fuse laterally to form full length filaments with a diameter of $b \approx 10$ nm, which form an orthogonal meshwork attached to the inner nuclear membrane with a lattice constant of ≈ 50 nm [2]. The scale bar is 1 μm. **b** The geometry of the orthogonal meshwork model, boundary conditions, and the coordinate system used in our simulations. The initial crack is oriented into the *x*-direction and the meshwork is loaded in one or both directions. The parameters *b*, *l*, and *h* denote the thickness, length, and width of the meshwork model; *d* is the lattice constant (≈50 nm) and *2a* is the initial crack length. **c** Schematic of the coarse-grain method used to model the meshwork. Mesoscopic particles or "beads" are used to describe full length filaments, where the equilibrated nearest neighbor distance is r_0 and an interbead potential fitted from stretching tests based on full atomistic modeling of intermediate filament is adopted. Inserted figures are snapshots of the atomic model of a segment of the 2B domain of an intermediate filament dimer under stretching, revealing molecular mechanisms of deformation

subunit, and is also known to alter the mechanical properties of the entire nuclear envelope [1, 6, 8, 10, 11]. Recent research revealed that defect accumulation in lamin also plays an important role in normal aging of human beings [12]. It has been shown in experimental studies that mutations and defects in nuclear lamina affect the nuclear envelope breakdown process during cell division, which can be a direct reason to cause illness. However, no studies have thus far linked the physical properties of the nuclear lamina to its underlying atomic and molecular structure and provided an explanation for its fundamental failure mechanism across multiple scales as has been done for other (e.g. engineered) materials [13–15].

In this paper, we investigate the mechanical failure of the nuclear lamina meshwork. We use a simple coarse-grain meshwork model with a realistic geometric and physical properties derived directly from the molecular scale to mimic the lamina meshwork of *Xenopus* oocytes [2, 16] as shown in Fig. 1a. We symmetrically fix one single layer of coarse-grain particles (so-called "beads") near the meshwork boundary and apply loading as shown in Fig. 1b. This setup resembles linear rails with guides clamped to the boundary as done in earlier experimental and computational studies [17, 18]. The mechanical response of each filament in the meshwork is modeled according to the mechanical response of a corresponding full atomistic model under tension. The deformation mechanisms revealed by a series of earlier atomistic modeling [19, 20] include: (a) a yielding regime (unfolding of alpha-helices), (b) a stiffening regime (alpha-to-beta structural transition), and (c) a secondary yielding regime (interprotein sliding under breaking of interprotein beta-strands). These fundamental mechanisms of deformation of each filament under loading are summarized in Fig. 1c.

2 Materials and Methods

2.1 Simulation Setup

This study uses a coarse-grain approach to implement a mechanical model of the intermediate filament meshwork

based on a hierarchical finer-trains-coarser multi-scale scheme. The entire structure of the nuclear envelope involves many other components, including the chromatin (resembling amongst others the genetic material) and cytoskeletal proteins. So far, however, only the amphibian oocytes' nuclear lamina has been isolated in experiments without association with chromatin [21]. Therefore the model we study here represents a first approximation to the realistic structure of other nuclear laminas, which may be more disordered and/or have slightly variegated structures. We also note that it differs from the physiological process of nuclear envelope breakdown process during cells' division since other chemical effects on the meshwork are not included in our work. This is motivated by the fact that it has been shown that an important function of the nuclear lamina is maintaining the mechanical integrity of cell nuclei, which is the focal point of this work [22].

The meshwork model shown in Fig. 1b includes 20 filaments in the *y*-direction (1 μm) and 100 filaments (5 μm) in the *x*-direction, with a crack-like defect added in the center to mimic a structural imperfection [9]. Filaments at the orthogonal corners are cross-linked by strong, covalent bonds which cannot break apart in our model. This assumption is based on the fact that the covalent bonds forming these cross-links are much stronger than the forces needed to cause filament rupture by sliding. All simulations reported here are carried out in two steps. First, we perform a relaxation during which we equilibrate the system. Relaxation is achieved by energy minimization, heating up the system from 0 to 300 K, then annealing the structure at a temperature of 300 K. Second, we perform a loading simulation during which we keep the system at 300 K using an *NVT* ensemble and apply a constant strain rate of 0.13 ns^{-1} to continuously increase the loading applied until the crack begins to travel through the entire meshwork. In studying the crack speed-to-applied strain relationships, we repeat our simulations, stop the increasing loading, fix the boundary at target strains, and record the steady-state crack propagation speeds.

2.2 Multi-scale Modeling Approach

The mesoscopic model is set up based on a combination of experimental and full atomic calculation data [2, 19]. We use a mesoscopic model describing each intermediate filament as a series of beads interacting according to nonlinear interparticle multibody potentials. The total energy is given by:

$$E_x = E_T + E_B, \tag{1}$$

The total energy is given by the sum over all pair-wise and three-body interactions:

$$E_T = \sum\nolimits_{\text{pair}} \varphi_T(r), E_B = \sum\nolimits_{\text{triplets}} \varphi_B(\theta) \tag{2}$$

where $\varphi_T(r)$ defines the pair-wise interaction potential between two bonded beads as a function of the distance r between the two beads, and $\varphi_B(\theta)$ defines the three-body interaction potential among three bonded beads as a function of the interior angle θ of the two pair bonds. Here, we approximate the nonlinear force-extension behavior under tensile loading with a multi-polynomial potential model that has been used successfully in an earlier study of deformation of single filaments found in the cytoplasm [23]. The tensile force between two particles (beads as illustrated in Fig. 1c) is described as:

$$F_T(r) = -\partial\varphi_T(r)/\partial r, \tag{3}$$

Where

$$\frac{\partial\varphi_T(r)}{\partial r} = \left[\exp\left(\frac{r-r_b}{r_b}\Xi\right)+1\right]^{-1}\begin{cases} k_1(r-r_0) & r<r_1 \\ R_1+k_2(r-r_1) & r<r_2 \\ R_2+k_3^1(r-r_2)+k_3^2(r-r_2)^2+k_3^3(r-r_2)^3 & r<r_3 \\ R_3 & r\geq r_3 \end{cases} \tag{4}$$

In Eq. 5, k_i and r_i are spring constants that derived directly from the force-extension curve of the tension test of full atomic model (as shown in Fig. 1c). r_0 is the equilibrium distance between pair beads. Alpha-helix domains within the filament are intact before the extension reaches r_1 and the slope of the force-extension curve is constant as defined by k_1. The extension beyond r_1 leads to the unfolding of the alpha-helix domains until they become nearly fully unfolded at r_2, and in this extension region the force-extension curve is linear with a slope of k_2. The third region before the extension of r_3 corresponds to the stiffening of the material because of the alpha–beta transition, and the nonlinearity of the force extension curve is expressed by a polynomial function with stiffness parameters k_3^1, k_3^2, and k_3^3. In the fourth region, the subunits within the filament slide against each other under a constant force. The parameters R_1, R_2, and R_3 are calculated from force continuity conditions.

Table 1 Geometric and numerical parameters for the coarse-grained computational model

Parameter and units	Numerical value
Equilibrium bead distance r_0 (in Å)	50
Critical distances r_1, r_1, r_3 (in Å)	75, 95, 138, 180
Tensile stiffness parameters k_1, k_2 (in kcal/mol/Å^2)	0.1595, 0.0324,
Tensile stiffness parameters for nonlinear region k_3^1(in kcal/mol/Å^2), k_3^2 (in kcal/mol/Å^3), k_3^3 (in kcal/mol/Å^4)	0.2044, 0.0146, 9.2465×10^{-4}
Force continuity conditions R_1, R_2, and R_3 (in kcal/mol/Å)	3.9877, 4.6357, 113.9364
Bond breaking distance r_b (in Å)	180
Equilibrium angle θ_0 (in rad)	π
Bending stiffness parameter k_B (in kcal/mol/rad^2)	169.51
Mass of each mesoscale particle (in amu)	230913
Switch function Ξ	300
Density ρ (in kg/m^3)	260

The value of these parameters are given in Table 1 without empirical fitting and are based directly on molecular modeling results. The Fermi–Dirac distribution function introduces two additional parameters r_b and Ξ [24]. The parameter r_b denotes the critical separation distance for breaking of the filament and the parameter Ξ describes the amount of smoothing around the breaking point (the smaller Ξ, the smoother the curve becomes). A similar strategy to model the potential near rupture for numerical analyses has been used in earlier studies. The numerical value of Ξ is set to a large value (Ξ=300) similar as in earlier work [24], and is chosen to mimic the steep descent characteristics of the force-extension curve as obtained from the molecular-level tetrameter model as depicted in Fig. 1c.

The bending energy is given by:

$$\varphi_B(\theta) = \frac{1}{2}k_B(\theta - \theta_0)^2 \tag{5}$$

with k_B relating to the bending stiffness of the intermediate filament EI through $k_B = 3EI/r_0$. The parameter EI relates to the intermediate filament persistence length L_p through $EI=L_pK_BT$, where K_B is the Boltzmann constant and T is the temperature.

The geometry of the meshwork is obtained from experimental observations of the nuclear lamina of *Xenopus* oocytes [2]. The meshwork is composed of two sets of near-orthogonal intermediate filaments with a lattice constant of d=50 nm, and we use d to normalize the crack length. We use a mesoscopic beads to model the each intermediate filament within the meshwork and define r_0=5 nm; this length is much smaller than the persistence length of the full length filament (on the order of 1 μm) and it is equal to the radius of the full length filament.

2.3 Damping

The damping effect is included in the model by considering the energy dissipation of the intermediate filament in motion caused by the viscosity of water environment. We note because of the small characteristic dimension of intermediate filaments, the Reynolds number ≪2,300 [25] and the drag force is approximately proportional to particle velocity (laminar flow). We use Stokes' law to estimate the drag force by [25]:

$$f_{\text{drag}} = -6\pi\mu Rv, \tag{6}$$

where $\mu = 8.6\times10^{-4}\text{Pa}\cdot\text{s}$ is the fluid viscosity constant of water at room temperature, R is the equivalent spherical radius of the mesoscopic bead, which equals to the radius of a sphere of equivalent volume given by [26]

$$R = \left(\frac{3}{16}b^2r_0\right)^{1/3} \tag{7}$$

with the geometry parameters of the mesoscopic bead (here, b=10 nm is the averaged diameter of intermediate filaments as measured in experimental work [1–4]), and we have R=4.5 nm. The parameter v denotes the relative velocity of the particle motion in a continuous viscous fluid.

2.4 Crack Propagation Velocity Measurements

The rupture length for bead–bead bonds is defined as $1.03r_b$, where the corresponding value of the Fermi–Dirac function is $<5\times10^{-5}$. The crack tip position is determined by finding the x-coordinate of the interior surface particle with maximum x or minimum x positions. We obtain the crack length by measuring the length between the two crack tips and average it over a small time interval to eliminate high-frequency fluctuations. We differentiate the half length with respect to time to obtain the crack propagation velocity for each of the two crack tips. To obtain the steady-state velocity of the crack, we ensure that the crack onset is within the region that the crack length satisfies $2L/d<35$; and we average the crack propagation speed as it reaches C beyond this region.

2.5 Computing Technique

The molecular simulations described here are carried out with a classical molecular dynamics approach by using an extended version of the LAMMPS code [27]. Visualization of atomic and mesoscopic models is carried out with the Visual Molecular Dynamics (VMD) software. Hydrogen bonds are defined to be within 5 Å for visualization purposes for atomic models for the inlays shown in Fig. 1 [28]. Visualization of the meshwork model is performed using MATLAB.

3 Results and Discussion

Figure 2 illustrates the failure mechanism of the meshwork with several snapshots shown for the case of uniaxial tensile crack loading (resembling mode I). To realize uniaxial tensile loading only ε_y is increased with a constant lateral strain ε_x=0. The meshwork is deformed and snapshots are taken at applied strains of ε_{y1}=37%, ε_{y2}=161%, ε_{y3}=162%, ε_{y4}=167%, ε_{y5}=172%, and ε_{y6}=174%. We observe no failure before ε_{y2}=161%, but the crack transforms from an initial horizontal orientation with a sharp edge pointed in the *x*-direction into a vertical orientation where the longest axis points in the *y*-direction. We observe that instead of forming a highly localized yield zone at the crack tip as typically seen in materials with a crack, all filaments in the direction in which tensile load is applied stretch significantly, and deformation extends over the entire specimen and is not limited to the crack tip region. A detailed analysis of the molecular state of these filaments reveals that the coiled-coil structure within each dimer building block has undergone molecular unfolding and a subsequent alpha–beta transition [20]. Catastrophic failure of the meshwork occurs once loading reaches ε_{y3}=162% and proceeds by rapid extension of the initial crack, which continues to propagate as a rapidly moving single crack as is shown in Fig. 2(III–VI). At the single filament scale, crack propagation is facilitated by the sliding apart of protein filaments after the transition into antiparallel beta-strands is completed, as is shown in Fig. 1c. Crack propagation occurs in a straight fashion into the *x*-direction without any branching or other instabilities.

We proceed with a detailed analysis of the dynamics of failure by crack propagation. We measure the steady-state crack speed *C* and find that *C*=18 m/s, *C*=21 m/s, *C*=

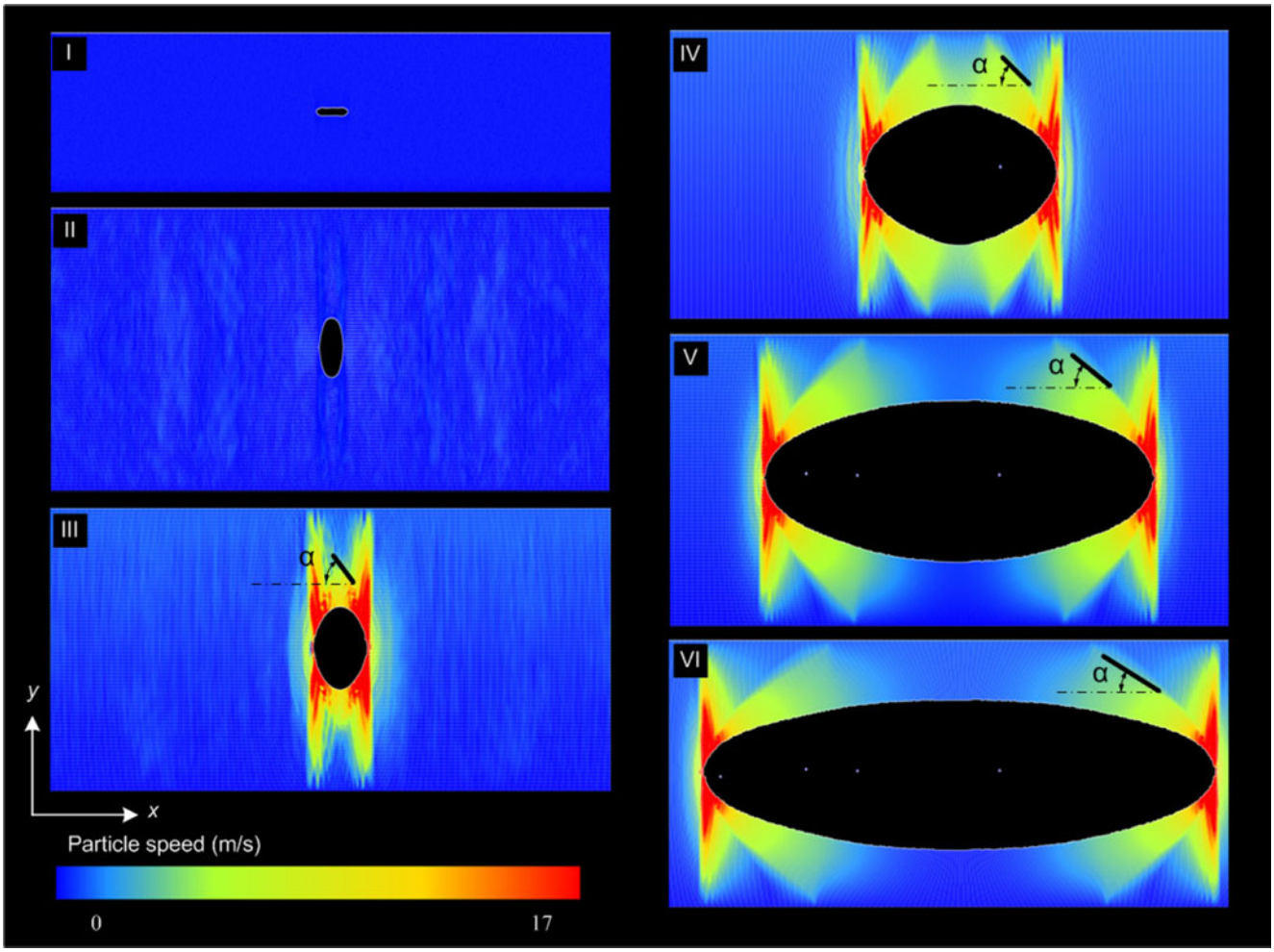

Fig. 2 Snapshots of deformation for a meshwork under uniaxial tensile (mode I) loading. The meshwork is deformed in the *y*-direction, with zero strain in the *x*-direction (ε_x=0) and *I*: ε_{y1}=37%, *II*: ε_{y2}=161%, *III*: ε_{y3}=162%, *IV*: ε_{y4}=167%, *V*: ε_{y5}=172%, and *VI*: ε_{y6}=174%; constant strain rate of 0.13 ns^{-1}. As loading is increased the crack shape changes from initially horizontally oriented (in *I*) to a vertically oriented shape (in *II* and following snapshots). As the crack propagates though the meshwork, two wave fronts emerge at the tip of the moving crack. One wave front is almost orthogonal to the crack propagation direction whereas the other one forms a well-defined cone. The angle α denotes the angle between the wave front and the crack propagation direction, and resembles a Mach cone

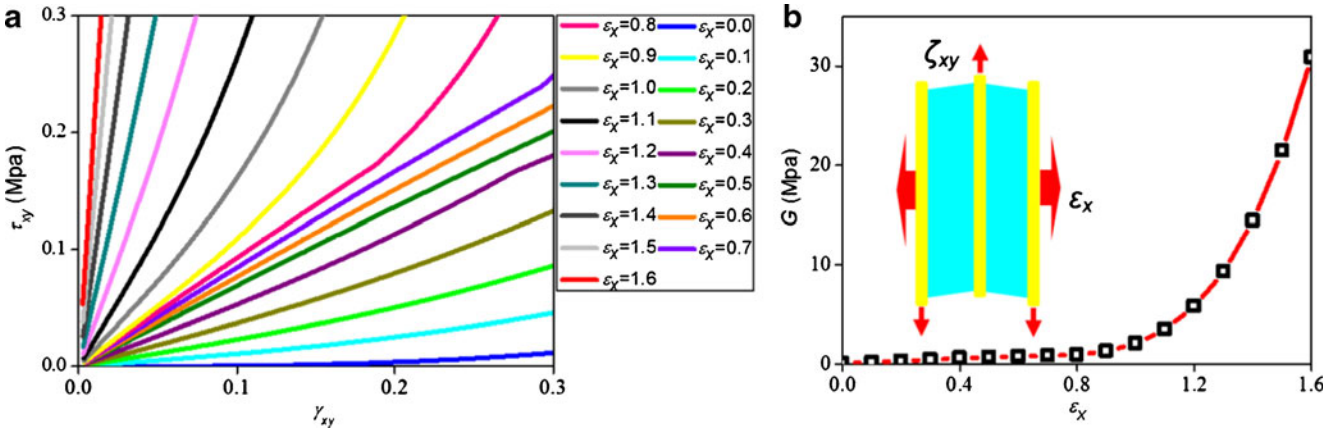

Fig. 3 Shear stress–strain relation at different axial loading ε_x (**a**) and shear modulus G as a function of axial loading ε_x (**b**). The results show that shear moduli G exponentially increases with increasing ε_x, and that a broad range of G can be achieved by altering ε_x

26 m/s, and C=28 m/s from small to large deformation, or from ε_{y3}, ε_{y4}, ε_{y5}, to ε_{y6}. We observe that as the crack moves through the material, two distinct wave fronts emanate from each crack tip as shown in Fig. 2(III–VI). One of the wave fronts resembles a shock front similar to a Mach cone, whereas the other one is almost orthogonal to the crack propagation direction. For the clearly visible shock wave, the measured angles between the wave front and the crack propagation direction are $\alpha \approx 53°$, 45°, 36°, and 33° for strains ε_{y3}, ε_{y4}, ε_{y5}, and ε_{y6}, respectively. Using these angles we estimate the wave speed associated with this particular shock wave based on the relation $\sin(\alpha) = C_0/C$, where C_0 is the characteristic wave speed that corresponds to the wave front with an angle of α. Based on this analysis we find C_0= 14, 15, 15, and 15 m/s of ε_{y3}, ε_{y4}, ε_{y5}, and ε_{y6}, respectively. The occurrence of the shock wave suggests that crack propagation occurs faster than a characteristic wave speed of the material, which is estimated to be around 14–15 m/s. According to continuum theory the Rayleigh-wave speed is given by $C_R \approx 0.923\sqrt{G/\rho}$, the shear-wave speed by $C_S = \sqrt{G/\rho}$ and the longitudinal wave speed is given by $C_L = \sqrt{3G/\rho}$, where G is the shear modulus of material and ρ is the averaged mass density of the meshwork model. To estimate the wave speeds as a function of applied strain for the protein meshwork considered here we apply a shear stress τ_{xy} on the boundary of a perfect meshwork model under tensile loading with a strain ε_x and record the shear stress over shear strain response as shown in Fig. 3a. We measure the shear modulus G of the meshwork material by computing the slope of the curve at the origin, with results shown in Fig. 3b. By continuously changing the value of ε_x we compute the shear modulus as a function of applied strain

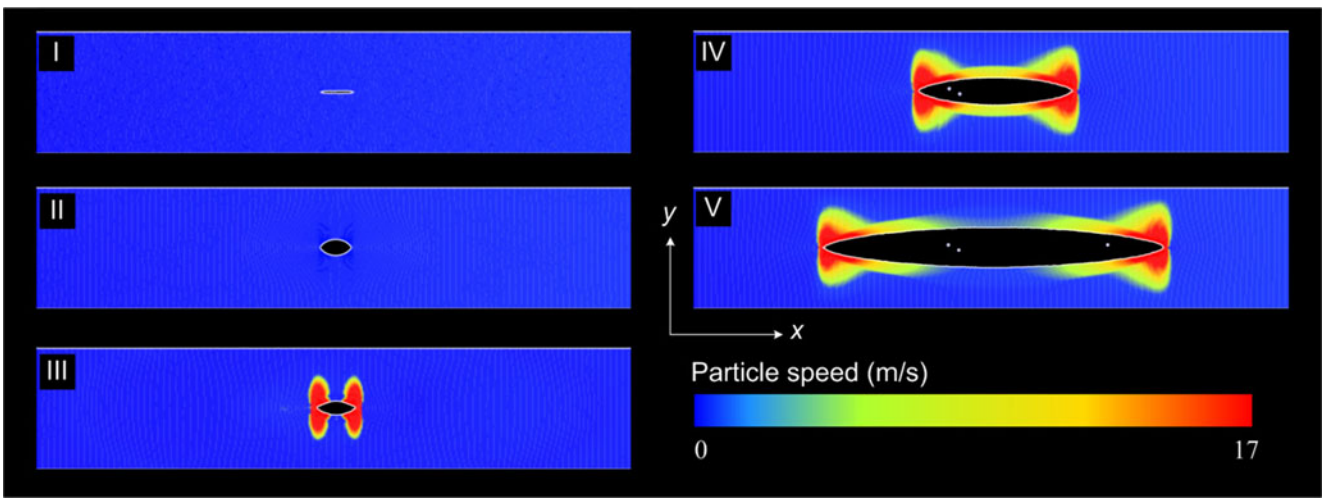

Fig. 4 Snapshots of deformation for a meshwork under equi-biaxial tensile loading. The meshwork is loaded by equi-biaxial tension in the x- and y-directions (loading condition shown in Fig. 1b); constant strain rate of 0.13 ns^{-1}. The meshwork is deformed with an applied strains of *I*: ε_{xy1}=37%, *II*: ε_{xy2}=161%, *III*: ε_{xy3}=162%, *IV*: ε_{xy4}= 165%, and *V*: ε_{xy5}=168%. The crack starts to propagate at the critical strain of ε_{xy3}=162%. Comparing to the uniaxial tension test shown in Fig. 2, there are two main differences: first, the initial x-direction crack does not flip to the y-direction before failure; second, no shock front or Mach cone is observed here

in the orthogonal direction. The analysis shows that the shear modulus and thus wave speeds increase as the loading is increased. For ε_x=0 the shear-wave speed and longitudinal wave speed in the *x*-direction are estimated to be C_L=25 m/s and C_S=14 m/s, respectively. We thus conclude that the shock wave front seen here corresponds to the shear-wave speed that it is caused by crack propagation faster than the speed of shear waves in the surrounding meshwork material, where $C>C_S$; representing intersonic crack propagation.

We suggest that the occurrence of intersonic crack propagation is due to the stiffening of the meshwork in the loading direction (*y*-direction), which results in an increased tangent modulus and as a result, in increased wave speeds and thus faster energy transport that can drive the crack to faster velocities [24, 29]. The shock front emerges because the wave speeds become anisotropic under uniaxial loading. The shear-wave speed and thus rate of energy transport in the *y*-direction increases as loading is increased due to the stiffening of the meshwork. Yet, the shear-wave speed in the *x*-direction is limited to a constant value, and hence, we observe the emergence of a shock front as the crack speed is driven to larger values in excess of the shear-wave speed. To test this hypothesis we carry out an equi-biaxial fracture test where the applied strain is identical in the *x*- and the *y*-direction, such that $\varepsilon_y=\varepsilon_x$. We expect a lack of shock wave fronts in this case due to the fact that under equi-biaxial loading the tangent moduli and thus wave speeds increase equally in both the *x*- and *y*-directions. The dynamics of meshwork failure under equi-biaxial tensile loading is depicted in Fig. 4. Two differences are immediately noticeable by comparing to the uniaxial tension case shown in Fig. 2. First, the initial *x*-direction-oriented crack does not flip to the *y*-direction. This is because under biaxial tension the strain in the filaments in both the *x*- and *y*-directions increase equally, preventing a change of the crack shape before failure. Second, in agreement with our hypothesis, no shock wave is observed upon failure initiation here in stark contrast to the case of uniaxial loading studied in Fig. 2.

The applied tensile strain is an important factor that affects the crack speed. For uniaxial loading (ε_x=0), we observe that the crack speed *C* is higher than the shear-wave speed C_S and increases linearly with ε_y and can slightly exceed C_L at the ultimate strain beyond ε_y=172% as shown in Fig. 5a. The maximum speed we observe under this loading condition is 32 m/s. We also investigate a case of multi-axial loading, where we keep ε_y=176% and change ε_x (note this case is different from the equi-biaxial loading discussed above since here generally $\varepsilon_y\neq\varepsilon_x$).We find that the crack speed increases significantly with increasing ε_x with a maximum speed of 280 m/s as shown in Fig. 5b. For comparison, we also plot the wave speeds C_R (the limiting speed predicted by linear-elastic fracture mechanics for a mode I crack) and C_L and find that they also increase with increasing strain in the *x*-direction, defining an upper and lower bound for the crack propagation speed. The observations made here show that the change in the applied strain in the nuclear lamina meshwork has significant implications on their dynamic fracture behavior. Indeed, it has been found in rupture experiments of rubber [17] that the crack propagation speed in a biaxial fracture test is between the C_R and C_L in

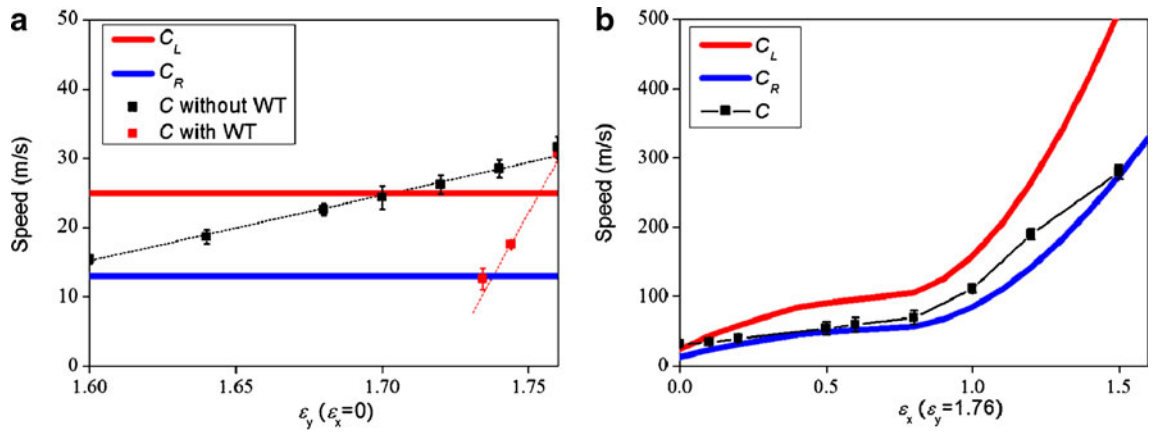

Fig. 5 Steady-state crack propagation speeds, Rayleigh-wave speed and longitudinal wave speed as a function of loading conditions. **a** Crack speed as a function of uniaxial loading strain ε_y. The crack speed is calculated from the derivative of half crack length *a* to the time once the value becomes steady; the fluctuations of the measured speed define the standard deviation as shown by the error bars. The Rayleigh-wave speed and longitudinal wave speed in the *x*-direction are calculated from the shear modulus *G* (as given in Fig. 3b) of a perfect meshwork model subjected to the corresponding loading condition. **b** Crack speed as a function of loading strain ε_x, with ε_y= 176% kept constant. The crack speed significantly increases as ε_x increases, and the crack speed is between the Rayleigh-wave speed and longitudinal wave speed in the plastic zone, which act as the lower and upper bound of the crack speed, respectively. The results shown here demonstrate that the crack propagation speed in the nuclear lamina is governed by the loading condition and the lateral strain ε_x is more dominant in governing the crack speed

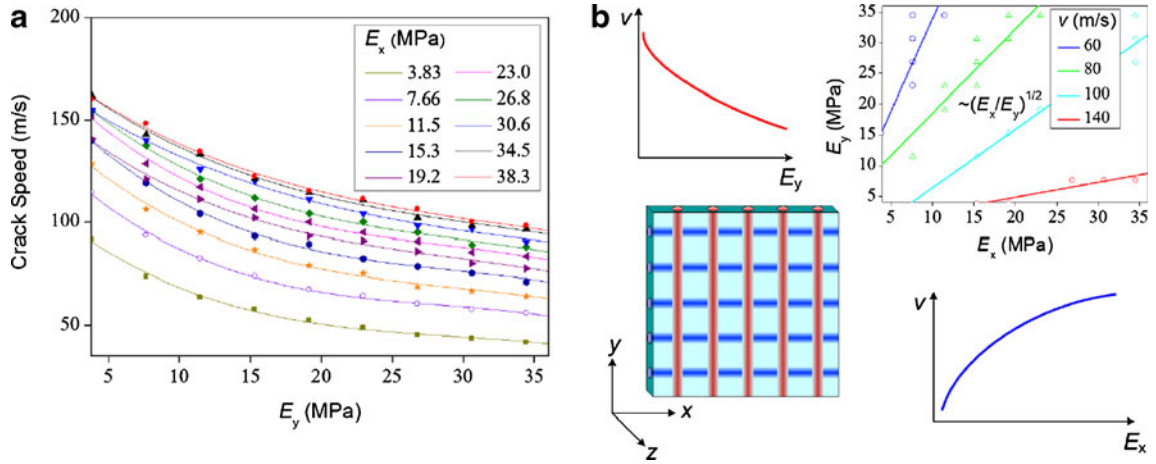

Fig. 6 Crack speed in an ideal anisotropic elastic meshwork. As the schematic of the geometry of the meshwork and definition of coordinates shows in panel **b**, the meshwork is composed of two kinds of linear-elastic filaments with different stiffnesses in the two orthogonal directions, which results in an anisotropic material with different moduli in the x- and y directions (E_x and E_y, respectively). The ultimate failure strain of each filament is set to be 176%, and crack speeds in this study correspond to the steady-state obtained at applied strain of ε_x=0 and ε_y=156%. **a**, Crack propagation speed as a function of E_x and E_y. The maximum modulus (found to be 38.3 MPa) here corresponds to the maximum tangent modulus of the nuclear lamina. **b** The crack speed decreases as E_y increases and increases as E_x increases, as illustrated by schematic plots in red and blue, respectively. Data points with same crack speeds are combined in groups as shown in the plot, which confirms that materials with same $\sqrt{E_x/E_y}$ feature the same crack speed. The results demonstrate that the crack propagation speed is governed by the ratio of the tangent material modulus in and perpendicular to the crack propagation direction, as given by $v \sim \sqrt{E_x/E_y}$. Therefore various crack propagation speeds are accessible via different ratios of $\sqrt{E_x/E_y}$ as can be achieved by different strain levels (ε_x, ε_y) in the real intermediate filament meshwork system

the rubber thin film, in agreement with our findings. For the specific cases considered here, the maximum speed reaches 22 times of the Rayleigh-wave speed at the relaxed zero-strain state.

We also study effect of damping due to the presence of water, by considering a viscous drag force. Under the presence of water the critical strain ε_C needed for crack initiation increases as the crack starts to propagate at a higher strain level. Once the crack starts to move, its steady speed starts with the Rayleigh-wave speed, increases in a steeper linear function with the increasing strain condition and reaches a maximum value as the same strain as in the model without solvent effect as shown in Fig. 5a. This result agrees with experimental observations that suggested that solvent viscosity slows down crack initiation as well as the propagation speed under constant pulling rates [30]. However, what we observed here is that the effect of viscosity vanishes at extreme loading conditions and does not affect the steady-state maximum crack speed in this case.

Unlike engineering materials such as metals, glass, and silicon, the nuclear lamina has a complex hierarchical structure as shown in Fig. 1. The change of the crack speed in the meshwork as a function of the applied strain is controlled by the stiffening behavior of individual intermediate filaments, which in turn is caused by characteristic changes in the molecular structure. As the secondary structure of each intermediate filament undergoes alpha-helix unfolding and an alpha–beta transition, the tangent shear stiffness of the meshwork experiences a significant increase, leading to a greater C_R, C_S, and C_L at larger deformation since $C_{R,S,L} \sim \sqrt{G}$. To directly test the hypothesis that the tangent stiffness controls crack dynamics, we measure the crack propagation speed in a linear-elastic meshwork system where we define a different stiffness for filaments in the x- and y-directions, respectively; where filaments are modeled by simple linear springs. This results in a meshwork with distinct elastic moduli E_x and E_y in the x- and y-directions, respectively. This mimics the anisotropic material properties that emerge when the loading in the x- and y-directions is different. Figure 6a shows the crack speed for varying combinations of elastic moduli, where crack propagation occurs in the x-direction and the moduli E_x and E_y are systematically changed. As can be inferred from Fig. 6a, the crack speed reaches the largest value as E_y decreases toward 0 MPa and E_x increases toward 38.3 MPa, which corresponds to the maximum tangent modulus of nuclear laminas before failure, as represented by Fig. 6b. The crack speed exponentially increases with the ratio $\sqrt{E_x/E_y}$ for variations of the elastic moduli in the orthogonal directions. This suggests that the crack propagation speed is governed by the ratio of the tangent material moduli in and perpendicular to the crack propagation direction, as given by $v \sim \sqrt{E_x/E_y}$. Therefore, various crack propagation speeds are accessible via different ratios of $\sqrt{E_x/E_y}$ as can be achieved by different strain levels (ε_x, ε_y) in the natural intermediate filament meshwork system.

4 Conclusion

Our results show that the speed of the crack propagation in intermediate filament meshwork is governed by the applied tensile strain in both the *x*- and *y*-directions. Under uniaxial loading tests, the crack speed exceeds the shear-wave speed, leading to a shock front or Mach cone at the crack tip, as shown in Fig. 2. We found that this phenomenon is caused by the material stiffening behavior, which is induced by the alpha-to-beta transition in the protein's secondary structure for the specific case considered here. This result is not limited to the particular material studied here but can have broad applications to many other protein or polymer materials with structural transitions and related stiffening (or softening) behavior under loading which may control the dynamics of material failure. Generally, the crack propagation speed reaches values greater than those predicted by simply considering the small-deformation moduli and associated wave speeds. It is noted that whereas intersonic crack speed contradicts conventional fracture theory for engineering materials, it agrees with the findings from earlier studies of nonlinear materials [24, 29, 31, 32].

The rapid propagation speed of the nuclear lamina meshwork seen here may reflect the behavior of cell nuclei during the cell division process from mechanical points of view. The occurrence of rapid fracture shows that once an extreme loading condition is reached, cracks propagate at a fast (here: intersonic) speed. This behavior may explain experimental observations that the nuclear envelope break-down processes during cell divisions are indeed found to occur at short time-scales and are irreversible. For human somatic cells, the chromatin is tightly associated with the nuclear lamina [21, 22], which may by some extent slow down crack propagation speeds. However, neither in situ nor in vitro experiments of somatic nuclear laminas are available yet. We hope that our study will trigger a broader interest in studying dynamic failure of cell nuclei, which may eventually facilitate the development of more complex somatic nuclear lamina models through the availability of additional experimental data.

More generally, the multi-scale method used here provides a powerful bridge to overcome the four orders of magnitudes difference in length scales to appropriately describe the characteristic of catastrophic failure in the nuclear lamina meshwork. Based on this method, it may also be possible to study the effect of diseases caused by point mutations and their effect on the mechanical and failure properties of nuclear laminas. The approach used here could also be applied to other hierarchical materials and provide insight into their dynamic failure mechanisms [33–37]. Additional work is needed to develop a solid theoretical foundation for fracture in discrete nonlinear systems as studied here and to provide a deeper investigation of the effect of solvent and chromatin on crack dynamics.

References

1. Herrmann, H., Bar, H., Kreplak, L., Strelkov, S. V., Aebi, U. (2007). Intermediate filaments: from cell architecture to nano-mechanics. *Nature Reviews Molecular Cell Biology, 8*(7), 562–573.
2. Aebi, U., Cohn, J., Buhle, L., Gerace, L. (1986). The nuclear lamina is a meshwork of intermediate-type filaments. *Nature, 323* (6088), 560–564.
3. Ishikawa, H., Bischoff, R., Holtzer, H. (1968). Mitosis and intermediate-sized filaments in developing skeletal muscle. *The Journal of Cell Biology, 38*(3), 538–555.
4. Chang, L., Shav-Tal, Y., Trcek, T., Singer, R. H., Goldman, R. D. (2006). Assembling an intermediate filament network by dynamic cotranslation. *The Journal of Cell Biology, 172*(5), 747–758.
5. Omary, M. B., Coulombe, P. A., McLean, W. H. I. (2004). Mechanisms of disease: intermediate filament proteins and their associated diseases. *The New England Journal of Medicine, 351* (20), 2087–2100.
6. van der Kooi, A. J., Bonne, G., Eymard, B., Duboc, D., Talim, B., Van der Valk, M., et al. (2002). Lamin A/C mutations with lipodystrophy, cardiac abnormalities, and muscular dystrophy. *Neurology, 59*(4), 620–623.
7. Dahl, K. N., Scaffidi, P., Islam, M. F., Yodh, A. G., Wilson, K. L., Misteli, T. (2006). Distinct structural and mechanical properties of the nuclear lamina in Hutchinson-Gilford progeria syndrome. *Proceedings Of The National Academy Of Sciences Of The United States Of America, 103*(27), 10271–10276.
8. Eriksson, M., Brown, W. T., Gordon, L. B., Glynn, M. W., Singer, J., Scott, L., et al. (2003). Recurrent de novo point mutations in lamin A cause Hutchinson-Gilford progeria syndrome. *Nature, 423*(6937), 293–298.
9. Djaczenk, W., Starzyk, H., Rzucidlo, Z. (1973). X-ray-irradiation induced changes of nuclear membrane of Kirkman-Robbins tumor-cells. *Experientia, 29*(1), 83–84.
10. Strelkov, S. V., Schumacher, J., Burkhard, P., Aebi, U., Herrmann, H. (2004). Crystal structure of the human lamin a coil 2B dimer: implications for the head-to-tail association of nuclear lamins. *Journal Of Molecular Biology, 343*(4), 1067–1080.
11. Buehler, M. J., & Yung, Y. C. (2009). Deformation and failure of protein materials in physiologically extreme conditions and disease. *Nature Materials, 8*(3), 175–188.
12. Scaffidi, P., & Misteli, T. (2006). Lamin A-dependent nuclear defects in human aging. *Science, 312*(5776), 1059–1063.
13. Herrmann, H., & Aebi, U. (1998). Intermediate filament assembly: fibrillogenesis is driven by decisive dimer-dimer interactions. *Current Opinion in Structural Biology, 8*(2), 177–185.
14. Carpinteri, A., & Pugno, N. M. (2008). Mechanics of hierarchical materials. *International Journal of Fracture, 150*(1–2), 221–226.
15. Ackbarow, T., Sen, D., Thaulow, C., Buehler, M. J. (2009). Alpha-helical protein networks are self-protective and flaw-tolerant. *PLoS ONE, 4*(6), e6015.
16. Qin Z, Buehler MJ (2011) Flaw tolerance of nuclear intermediate filament lamina under extreme mechanical deformation. ACS Nano. doi:10.1021/nn200107u.
17. Petersan, P. J., Deegan, R. D., Marder, M., Swinney, H. L. (2004). Cracks in rubber under tension exceed the shear wave speed. *Physical Review Letters, 93*(1), 015504.
18. Sen, D., Thaulow, C., Schieffer, S. V., Cohen, A., Buehler, M. J. (2010). Atomistic study of crack-tip cleavage to dislocation emission

transition in silicon single crystals. *Physical Review Letters, 104*(23), 235502.
19. Qin, Z., Kreplak, L., Buehler, M. J. (2009). Hierarchical structure controls nanomechanical properties of vimentin intermediate filaments. *PLoS ONE, 4*(10), e7294.
20. Qin, Z., & Buehler, M. J. (2010). Molecular dynamics simulation of the alpha-helix to beta-sheet transition in coiled protein filaments: evidence for a critical filament length scale. *Physical Review Letters, 104*(19), 198304.
21. Goldberg, M. W., Huttenlauch, I., Hutchison, C. J., Stick, R. (2008). Filaments made from A- and B-type lamins differ in structure and organization. *Journal of Cell Science, 121*(2), 215–225.
22. Dahl, K. N., Kahn, S. M., Wilson, K. L., Discher, D. E. (2004). The nuclear envelope lamina network has elasticity and a compressibility limit suggestive of a molecular shock absorber. *Journal of Cell Science, 117*(20), 4779–4786.
23. Bertaud, J., Qin, Z., Buehler, M. J. (2010). Intermediate filament-deficient cells are mechanically softer at large deformation: a multi-scale simulation study. *Acta Biomaterialia, 6*(7), 2457–2466.
24. Buehler, M. J., & Gao, H. J. (2006). Dynamical fracture instabilities due to local hyperelasticity at crack tips. *Nature, 439*(7074), 307–310.
25. Batchelor, G. K. (1967). *An introduction to fluid dynamics*. Cambridge: University Press.
26. Jennings, B. R., & Parslow, K. (1988). Particle-size measurement—the equivalent spherical diameter. *Proceedings of the Royal Society of London Series A-Mathematical Physical and Engineering Sciences, 419*(1856), 137–149.
27. Plimpton, S. (1995). Fast parallel algorithms for short-range molecular-dynamics. *Journal of Computational Physics, 117*(1), 1–19.
28. Humphrey, W., Dalke, A., Schulten, K. (1996). VMD: visual molecular dynamics. *Journal of Molecular Graphics, 14*(1), 33–38.
29. Buehler, M. J., Abraham, F. F., Gao, H. J. (2003). Hyperelasticity governs dynamic fracture at a critical length scale. *Nature, 426*(6963), 141–146.
30. Baumberger, T., Caroli, C., Martina, D. (2006). Solvent control of crack dynamics in a reversible hydrogel. *Nature Materials, 5*(7), 552–555.
31. Pugno, N. M. (2006). Dynamic quantized fracture mechanics. *International Journal of Fracture, 140*(1–4), 159–168.
32. Pugno, N. M., & Ruoff, R. S. (2004). Quantized fracture mechanics. *Philosophical Magazine, 84*(27), 2829–2845.
33. Wegst, U. G. K., & Ashby, M. F. (2004). The mechanical efficiency of natural materials. *Philosophical Magazine, 84*(21), 2167–2181.
34. Espinosa, H. D., Rim, J. E., Barthelat, F., Buehler, M. J. (2009). Merger of structure and material in nacre and bone—perspectives on de novo biomimetic materials. *Progress in Materials Science, 54*(8), 1059–1100.
35. Nukala, P. K., & Simunovic, S. (2005). Statistical physics models for nacre fracture simulation. *Phys Rev E Stat Nonlin Soft Matter Phys, 72*(4 Pt 1), 041919.
36. Pugno, N. M. (2006). Mimicking nacre with super-nanotubes for producing optimized super-composites. *Nanotechnology, 17*(21), 5480–5484.
37. Qin, Z., Feng, X. Q., Zou, J., Yin, Y. J., Yu, S. W. (2007). Superior flexibility of super carbon nanotubes: molecular dynamics simulations. *Applied Physics Letters, 91*(4), 043108.